Supplementary information for:

Reduced Northern mid-latitude carbon sink estimates from atmospheric CO_2 data

Zhiqiang Liu[1,2], Ning Zeng[3,4], Yun Liu[5,6], Jun Wang[7], Pengfei Han[8,1], Qixiang Cai[1]

[1]Laboratory of Numerical Modeling for Atmospheric Sciences & Geophysical Fluid Dynamics, Institute of Atmospheric Physics, Chinese Academy of Sciences, Beijing, China
[2]University of Chinese Academy of Sciences, Beijing, China
[3]Dept. of Atmospheric and Oceanic Science, University of Maryland, USA
[4]Earth System Science Interdisciplinary Center, University of Maryland, USA
[5]Dept. of Oceanography, Texas A & M University, College Station, TX, USA
[6]Geochemical and Environment Research Group, Texas A&M University, College Station, TX, USA
[7]International Institute for Earth System Science, Nanjing University, Nanjing, China
[8]Carbon Neutrality Research Center, Institute of Atmospheric Physics, Chinese Academy of Sciences, Beijing, China

Corresponding authors: Zhiqiang Liu (liuzhiqiang@mail.iap.ac.cn) and Ning Zeng (zeng@umd.edu)

1. CO_2 Data

1.1 Satellite retrieval from OCO-2

In this study, we use both surface and satellite observations. We use a 10-second averaged dataset of the Orbiting Carbon Observatory-2 (OCO-2) based on the ACOS algorithm of version 10[1,2]. This dataset is used in the OCO-2 flux model intercomparison project of version 10. And we only use the good-quality land-nadir and land-glint data (Fig. S1) following the OCO2MIP protocol.

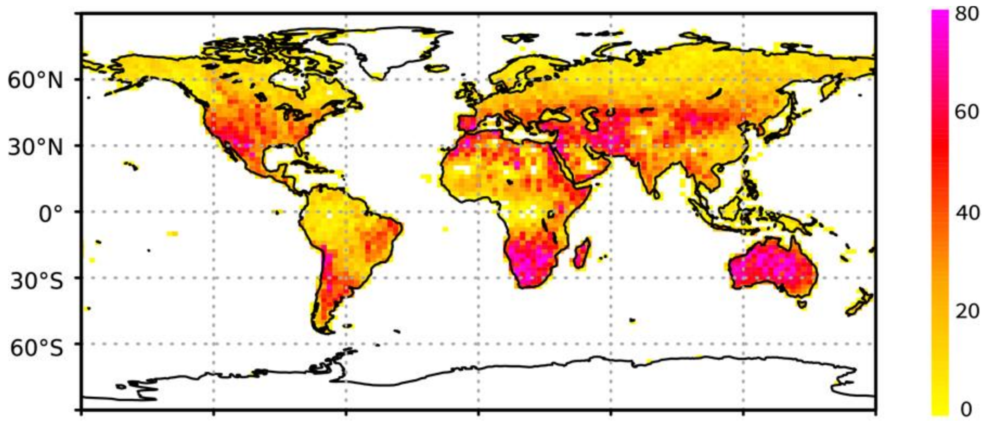

Figure S1: The total number of the 10-second averaged OCO-2 land-nadir and land-glint observations of 2015 in each 2×2.5 grid point.

1.2 Surface observation from ObsPack GLOBALVIEWplus

The surface in-situ and flask observations are obtained from the obspack_co2_1_GLOBALVIEWplus_v8.0_2022-08-27 dataset[3]. The v8.0 ObsPack data are processed under the X2019 WMO scale, while the ACOS v10 OCO-2 data are generated based on the X2007 WMO scale. To maintain the consistency between the two types of observations, we corrected the ObsPack data back to the X2007 scale. Fig. S2 shows the surface CO_2 observation network. Sites within the dataset that can represent large-scale CO_2 signals are selected. We only use the data from 2:00 to 4:00 local solar time for in-situ sites at the mountaintop. We only use the data from 14:00 to 16:00 local solar time for the other in-situ sites. After the data selection process, the data within an hour are averaged into one observation to match with the model ensemble forecast. An important part of the observations is the observation error. Typically, the observation error includes instrument error and representative error (or model-data mismatch error). To estimate the representative error, we first use the *ccgcrv* algorithm to derive the detrended and deseasonalized series at each site[4,5]. Based on the series, we calculate the 14-day moving standard deviation as the proxy of the representative error. Overall, the temporal mean representative error ranged from less than 0.1 ppm near the south pole sites to over 10 ppm at some northern midlatitude tower sites. Accurate interpolation of the model forecast to the location of observations at different altitudes is a critical process[6]. Within the ObsPack, the altitude of each site is provided. Then, we calculate each station's intake height by subtracting the transport model terrain height from the observation altitude. Based on this strategy, some mountain top stations (e.g., MLO) are located over 1000 meters above the ground in the transport model.

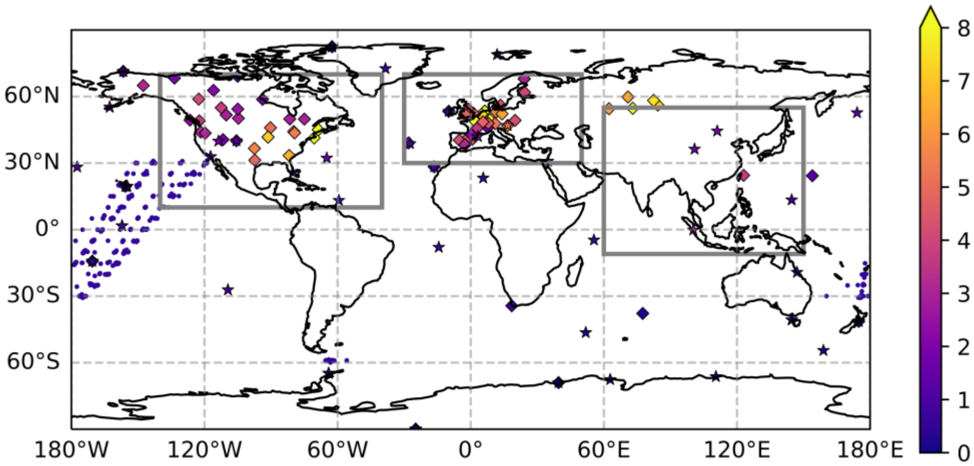

Figure S2: The surface observation network used in this study. The diamonds denote the in-situ sites, the pentagrams denote the flask sampling sites, and the small circles denote the shipboard flask samples. The color indicates the representative error assigned to each site and sample. Notes that the shipboard flask samples are assigned with a fixed 0.5 ppm representative error. The three gray rectangles denote the N. America, Europe, and E. Asia regions.

2. Inversion system

2.1 GEOS-Chem model

The Carbon in Ocean-Land-Atmosphere (COLA) is an ensemble-based CO_2 data assimilation system used in this study. The atmospheric transport model (ATM) used in COLA is the GEOS-Chem of version 13.0.2[7,8]. It is convenient to conduct ensemble simulations using a single GEOS-Chem program using a YAML list to define the tracers. CO_2 is a passive tracer, and the chemical reaction and radiation modules in GEOS-Chem are closed to speed up the model simulation. GEOS-Chem can run at global $4° \times 5°$ and $2° \times 2.5°$ resolutions using coarse GEOS-FP or MERRA-2 meteorological fields from NASA Global Modeling and Assimilation Office[9]. The GEOS-Chem development group recommends using the MERRA-2 data, and COLA uses the MERRA-2 as the default meteorological field. The parent model of MERRA-2 is the Goddard Earth Observing System (GEOS) model using the cubed-sphere grid. The analysis outputs are regrided to the latitude-longitude grid at $0.5° \times 0.625°$ resolution. The classic GEOS-Chem is paralleled using OpenMP with shared memory. Thus, it is prohibitive to run the global GEOS-Chem at the native $0.5° \times 0.625°$ resolution, and the native high-resolution simulation is usually conducted at a region of interest. The GEOS-Chem allows users to run at a customized domain but requires downloading large global meteorological files. The GEOS-Chem developers predefined three domains of meteorological fields in North America, Europe, and East Asia to facilitate high-resolution studies. In the previous COLA system, inversions could only conduct at global coarse resolution. This study updated COLA with the high-resolution inversion capability in the three nested domains.

2.2 A local transform ensemble Kalman filter (LETKF) and a constrained ensemble Kalman filter (CEnKF)

we use the four-dimensional local ensemble transform Kalman filter (LETKF) as the main DA algorithm. An assimilating a priori as special observation (AAPO) algorithm is embedded in the LETKF process. Moreover, a constrained ensemble Kalman filter is applied after the LETKF process. The LETKF is configured to digest asynchronous hourly CO_2 observations within the observation window (OW) of 7 days, and to update the flux parameter and CO_2 state at the end of the assimilation window (AW) of 1 day. The overall LETKF algorithm is summarized as follows:

$$\bar{\mathbf{x}}^{\mathrm{a}} = \bar{\mathbf{x}}^{\mathrm{b}} + \mathbf{X}^{\mathrm{b}}\bar{\mathbf{w}} \quad (1.)$$

$$\bar{\mathbf{w}} = \widetilde{\mathbf{P}}^{\mathrm{a}}\left(\mathbf{Y}^{\mathrm{b}}\right)^{\mathrm{T}}\mathbf{R}^{-1}\left(\mathbf{y}^{\mathrm{o}} - \bar{\mathbf{y}}^{\mathrm{b}}\right) \quad (2.)$$

$$\widetilde{\mathbf{P}}^{\mathbf{a}} = [\left(\mathbf{Y}^{\mathrm{b}}\right)^{\mathrm{T}}\mathbf{R}^{-1}\left(\mathbf{Y}^{\mathrm{b}}\right)+(\mathrm{K}-1)\mathbf{I}]^{-1} \quad (3.)$$

$$\mathbf{X}^{\mathbf{a}} = \mathbf{X}^{\mathrm{b}}[(\mathrm{K}-1)\widetilde{\mathbf{P}}^{\mathrm{a}}]^{\frac{1}{2}} \quad (4.)$$

Where $\mathbf{x} = [\mathbf{c}, \mathbf{f}]^{\mathbf{T}}$ that **c** is the CO_2 state and **f** is the flux parameter; the background and analysis error uncertainties are represented by the perturbations of background ($\mathbf{X}^{\mathrm{b}} = \mathbf{x}_{\mathrm{k}}^{\mathrm{b}} - \bar{\mathbf{x}}_{\mathrm{k}}^{\mathrm{b}}$)and analysis ($\mathbf{X}^{\mathrm{a}} = \mathbf{x}_{\mathrm{k}}^{\mathrm{a}} - \bar{\mathbf{x}}_{\mathrm{k}}^{\mathrm{a}}$) ensembles, respectively; $\mathbf{x}_{\mathrm{k}}^{\mathrm{b}}$ and $\bar{\mathbf{x}}^{\mathrm{b}}$ are the background and its mean, respectively; $\mathbf{x}_{\mathbf{k}}^{\mathbf{a}}$ and $\bar{\mathbf{x}}^{\mathbf{a}}$ are the analysis ensemble and its mean, respectively; $\mathbf{y}^{\mathrm{o}}=[\mathbf{y}_{\mathbf{CO_2}}^{\mathbf{o}}, \mathbf{y}_{\mathbf{ap}}^{\mathbf{o}}]$ is the assimilated observations that include common CO_2 observation and a priori (ap); and $\mathbf{y}_{\mathrm{k}}^{\mathrm{b}}$ **and** $\bar{\mathbf{y}}^{\mathrm{b}}$ are the forecast observations and their mean, respectively. $\mathbf{y}_{\mathrm{k}}^{\mathrm{b}} = \mathbf{h}(\mathbf{x}_{\mathrm{k}}^{\mathrm{b}})$ projects the background from the model space to the observation space with the observation operator **h**. Here $\mathbf{X}^{\mathrm{b}}\bar{\mathbf{w}}$ is the ensemble mean analysis increment applied to each ensemble member, with **R** denoting the observation error covariance, $\widetilde{\mathbf{P}}^{\mathrm{a}}$ is the analysis error covariance, K is the number of ensemble members, and **I** is the identity matrix. LETKF simultaneously assimilates all observations within a certain distance at each model grid point. We set the localization radium of 4000 kilometers for CO_2 observations and small localization radium for a priori. After the LETKF process, we conduct a CEnKF step to maintain the global mass balance:

$$\bar{\mathbf{c}}^{\mathrm{a}+} = \bar{\mathbf{c}}^{\mathrm{a}} + \mathbf{E}^{\mathrm{a}}(\mathbf{h}'\mathbf{E}^{\mathrm{a}})^{\mathrm{T}}(\mathbf{h}'\mathbf{E}^{\mathbf{a}}(\mathbf{h}'\mathbf{E}^{\mathrm{a}})^{\mathrm{T}})^{-1}\left(\mathbf{h}'\bar{\mathbf{c}}^{\mathrm{b}} - \mathbf{h}'\bar{\mathbf{c}}^{\mathrm{a}}\right) \quad (5.)$$

where $\bar{\mathbf{c}}^{\mathrm{a}+}$ is the CEnKF CO_2 ensemble mean. $\bar{\mathbf{c}}^{\mathrm{a}}$ is the LETKF ensemble mean of CO_2. $\mathbf{E}^{\mathrm{a}}$ is the ensemble perturbation of CO_2 after the LETKF process. CEnKF defines the “observations” as the truth with $\mathrm{r} = 0$ to meet the mass conservation purpose.

2.2 Ensemble uncertainty

For the 4-year period, EXP-high gives a small uncertainty of ~0.08 GtC yr^{-1} for the sum of the three regions. Such small uncertainty estimation significantly differs from some of the traditional inversion methods. Traditional methods usually optimize the flux at weekly or monthly timestep and assume that flux in each window is independent. In COLA, there is a strong temporal correlation between each 1-day assimilation window based on the persistent forecast hypothesis. The ensemble uncertainty at a given grid or region and during a given period is defined as,

$$\boldsymbol{\sigma}_{\mathrm{i,t1,t2}}^{\mathrm{a}} = \sqrt{\frac{\sum_{\mathrm{n}}(\boldsymbol{f}_{\mathrm{i,t1,t2,n}}^{\mathrm{a}} - \bar{\boldsymbol{f}}_{\mathrm{i,t1,t2}}^{\mathrm{a}})^2}{\mathrm{N}-1}}, \quad (6.)$$

where $\boldsymbol{f}_{\mathrm{i,t1,t2,n}}^{\mathrm{a}}$ is the total analysis flux of the nth ensemble member at a given grid-point or region i during the period from t1 to t2; $\bar{\boldsymbol{f}}_{\mathrm{i,t1,t2}}^{\mathrm{a}}$ is the ensemble mean of analysis flux; N denotes the ensemble size. COLA estimates an ensemble of high-frequency and grided fluxes. The temporal evolution of the grided fluxes of each ensemble member represents the possible trajectory under the guidance of observations. Thus, each ensemble member represents a good estimation consistent with the observations. In other words, since each ensemble member is a perturbation from the ensemble means, an ensemble member is not expected to be persistently smaller or larger than the ensemble mean. Thus, when averaging the high-frequency flux to the annual scale, the relative difference between each ensemble member will be reduced dramatically.

At each 1-day assimilation step, the ensemble spread will be reduced from background ensemble to analysis ensemble. Fig. S3 shows the averaged daily ensemble spread reduction ratio in 2015. The strong spread reduction occurs in the high-latitude area of North America, where the observation coverage is denser than the other area.

3. Results

3.1 Fluxes at annual and seasonal scales

Fig. S4 and S5 show the annual natural fluxes and the annual biospheric flux from 2015 to 2018 in the three model domains and in the nations, respectively. Similar to Fig. 1b and Table 1, the biases in EXP-mid and EXP-low are also shown in each year's estimates. The interannual variation in the three experiments is consistent with each other. In addition to Fig 1a and 1b, we show the spatial distribution of the 4-year mean flux of EXP-mid and EXP-low in Fig. S6 and Fig. S7. The 4-year mean biases in EXP-low are more significant than in EXP-mid.

Fig. S8 shows the national seasonal cycle. Compared to EXP-high, EXP-low, EXP-mid, and the ensemble mean of OCO2MIP show a consistent underestimation of the seasonal amplitude in all of the four nations. The underestimation of seasonal strength also shows in most grids (Fig. S8, S10), with more carbon release during the decaying seasons than carbon sink during the growing seasons (Fig. 2, S11).

3.2 CO_2 distribution

Fig. S12 shows the surface CO_2 distribution of EXP-high and the boundary inflow from EXP-mid in January and July 2018. The CO_2 gradient between the domain edges of the three regions is consistent with the boundary inflow, indicating that the ensemble boundary condition is appropriately assigned.

Fig. S13~S18 are additional information to Fig. 3. They show the vertical-latitude distribution of CO_2 and the biases of EXP-mid and EXP-low for different seasons or annual mean. For example, in E. Asia, the biases within the 850 hpa pressure level are positive for both summer and winter (Fig. S16~S18), which is consistent with Fig. 3.

4. Evaluation against independent observations

We evaluated the results against independent vertical profiles in N. America. The bias of EXP-high is smaller than EXP-mid and EXP-low in different seasons and altitude (Fig. S19).

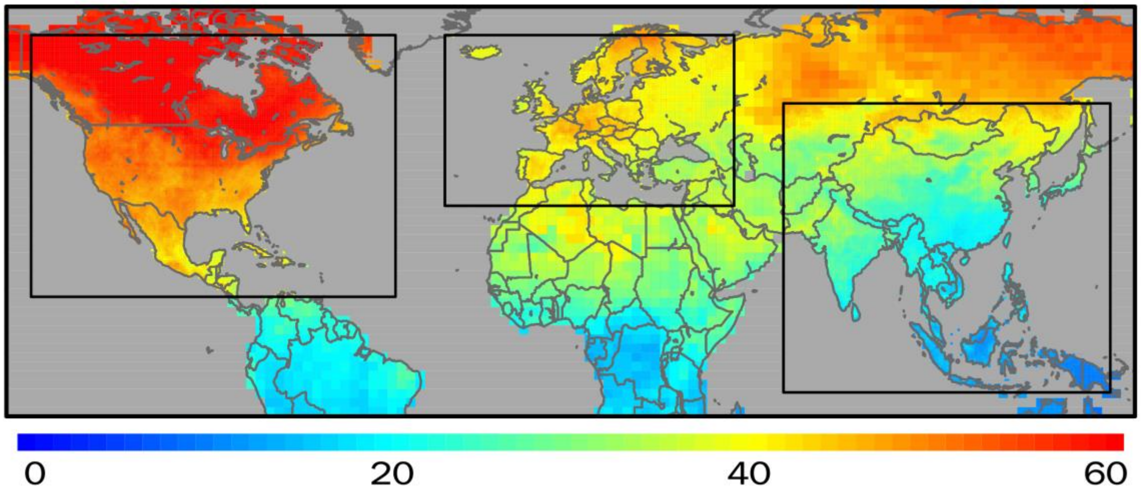

Figure S3: Averaged daily ensemble spread reduction ratio in 2015. The ratio is calculated by subtracting the ensemble spread difference before and after the assimilation step by the ensemble spread before the assimilation step.

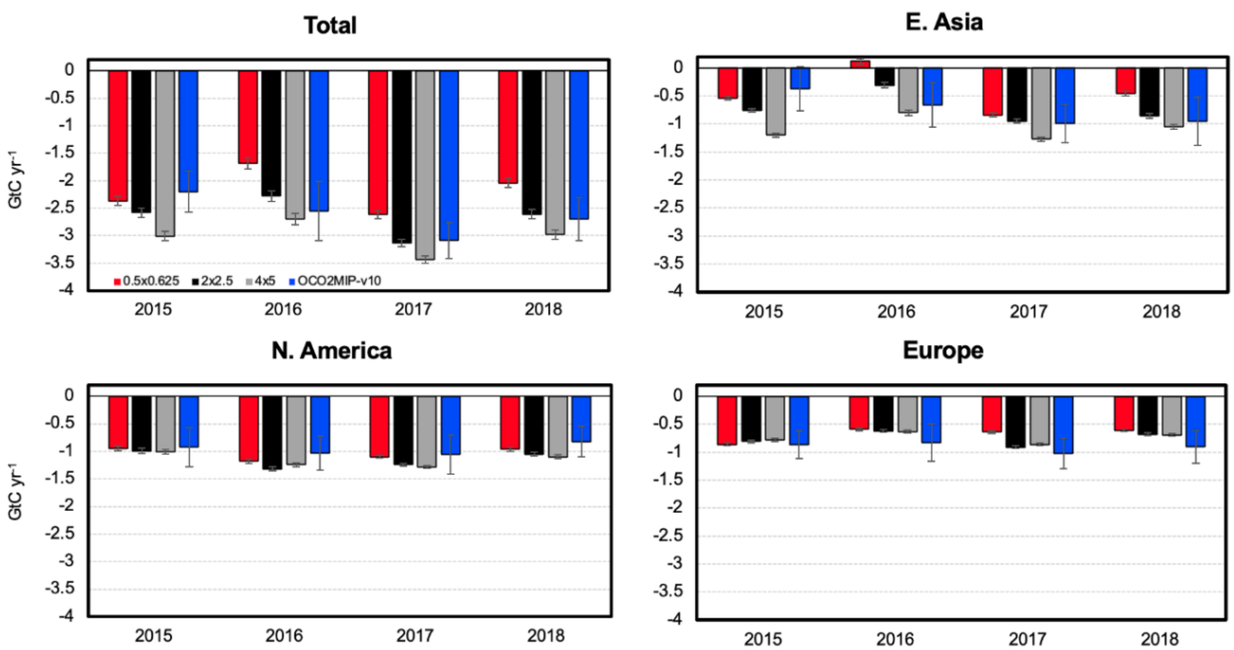

Figure S4: Annual natural fluxes of terrestrial and ocean carbon fluxes (GtC yr^{-1}) in E. Asia, N. America, Europe, and the sum of the three regions from 2015 to 2018.

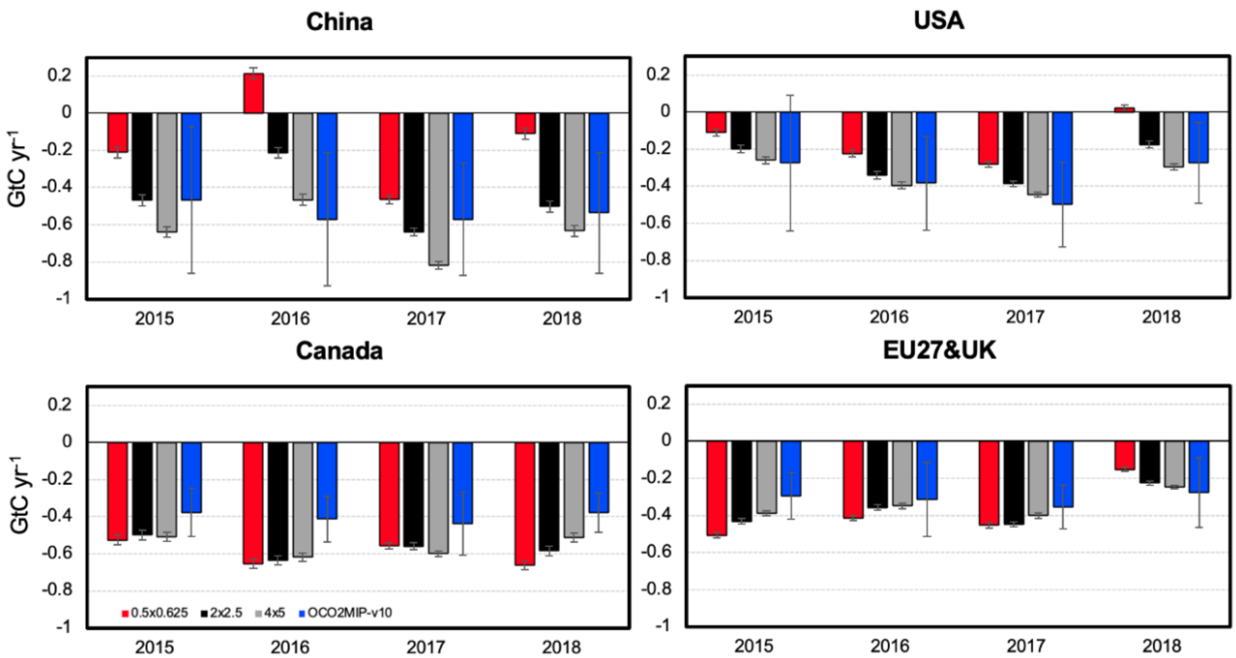

Figure S5: Annual terrestrial carbon fluxes (GtC yr^{-1}) in China, USA, Canada, and EU27&UK from 2015 to 2018.

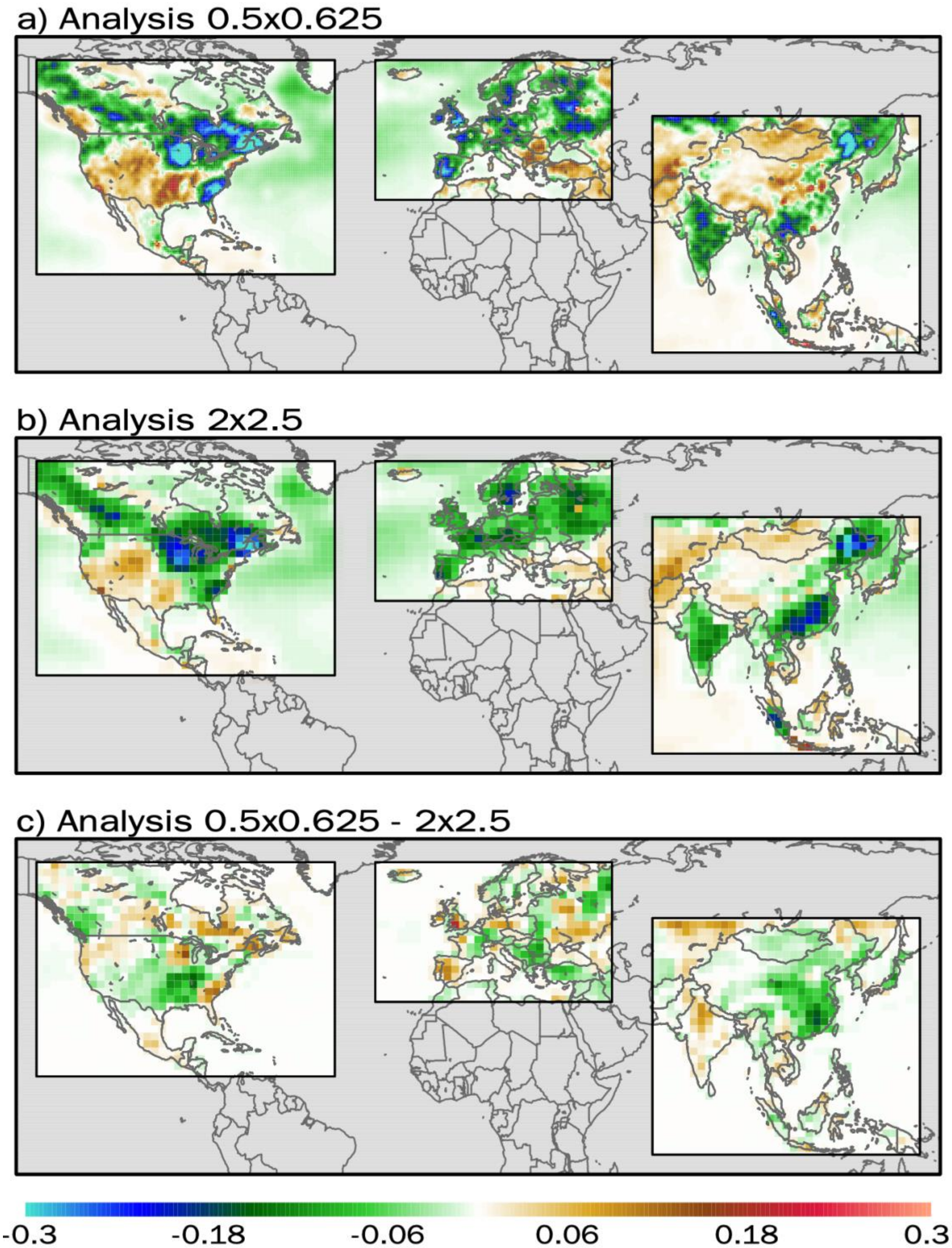

Figure S6: Terrestrial and ocean carbon fluxes in N. America, E. Asia, and Europe for 2015~2018. Annual mean spatial pattern of analysis of carbon fluxes (KgC m^{-2} yr^{-1}) from a) EXP-high at 0.5° ×0.625° resolution and EXP-mid at 2° ×2.5°. c) Annual mean difference between EXP-mid and EXP-high (KgC m^{-2} yr^{-1}).

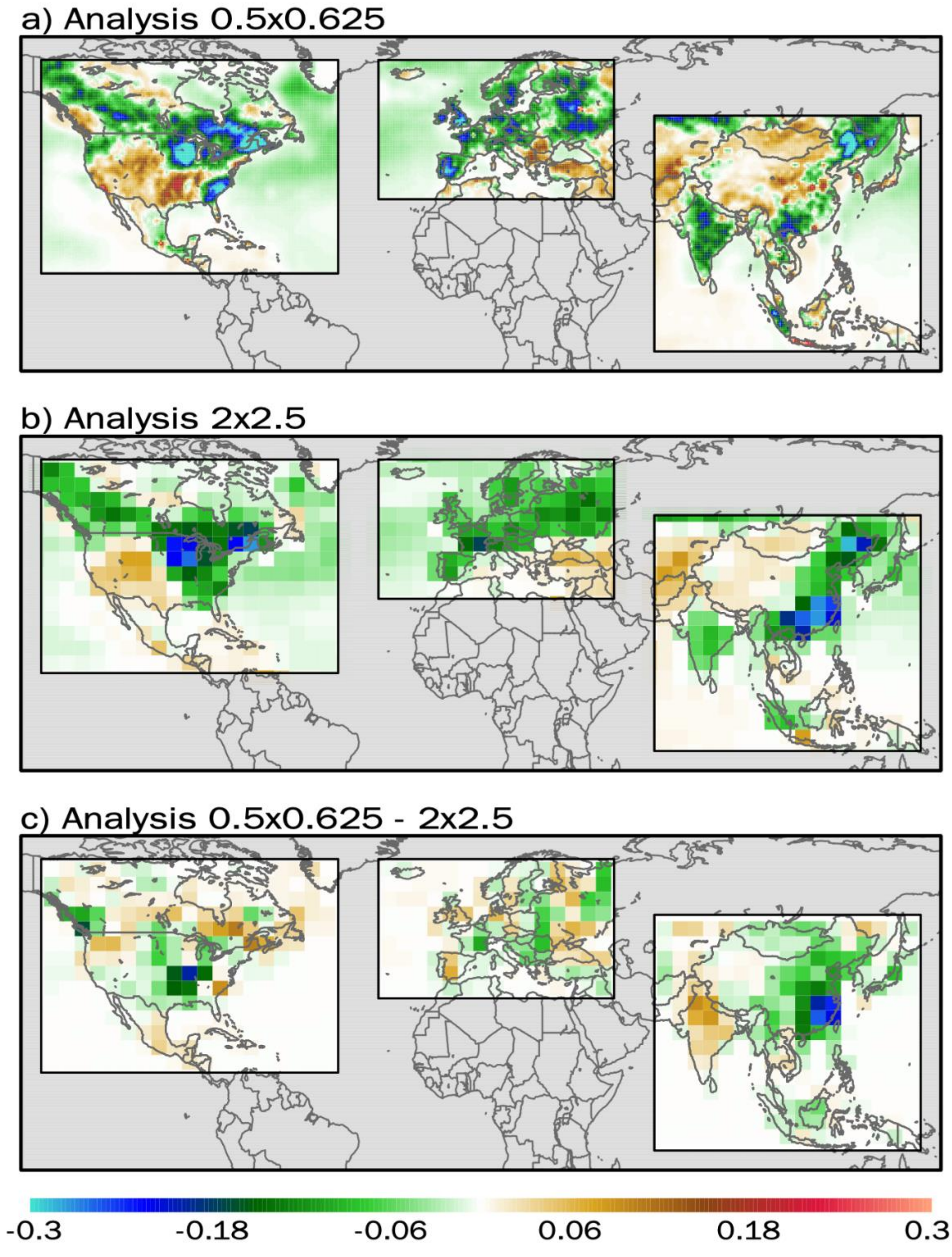

Figure S7: Terrestrial and ocean carbon fluxes in N. America, E. Asia, and Europe for 2015~2018. Annual mean spatial pattern of analysis of carbon fluxes (KgC m^{-2} yr^{-1}) from a) EXP-high at 0.5° ×0.625° resolution and EXP-low at 4° ×5°. c) Annual mean difference between EXP-low and EXP-high (KgC m^{-2} yr^{-1}).

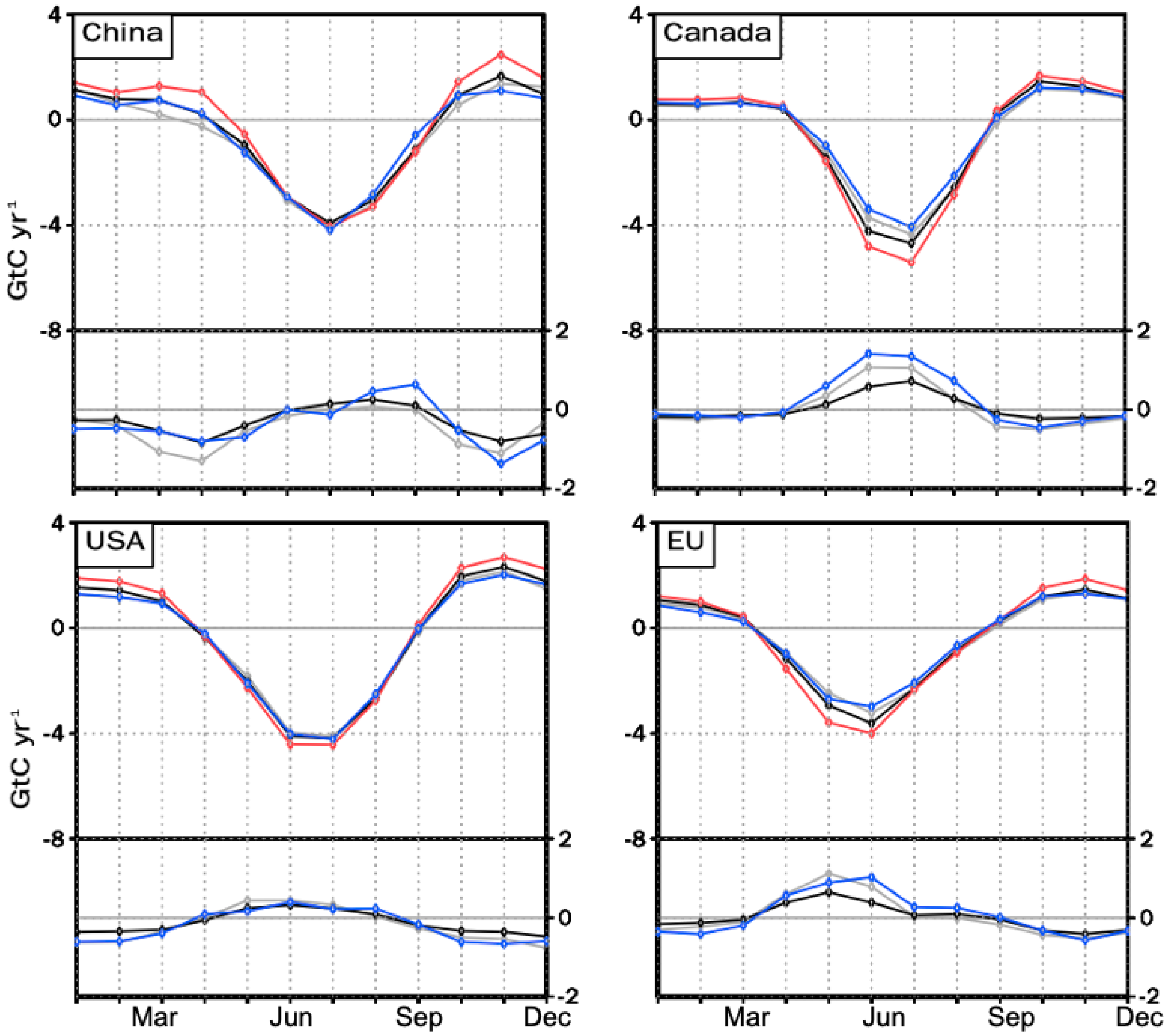

Figure S8: Climatology seasonal cycle of terrestrial carbon fluxes in China, USA, Canada, and EU27&UK for 2015~2018. In each figure, the red, black, gray, and blue lines with diamonds marked on are EXP-high at 0.5° ×0.625° resolution, EXP-mid at 2° ×2.5° resolution, EXP-low at 4° ×5° resolution, and the OCO2MIP-v10 ensemble mean, respectively. The upper lines in each subplot are the original seasonal cycle, and the bottom lines are the differences of EXP-mid, EXP-low, and the OCO2MIP-v10 ensemble mean compared to EXP-high.

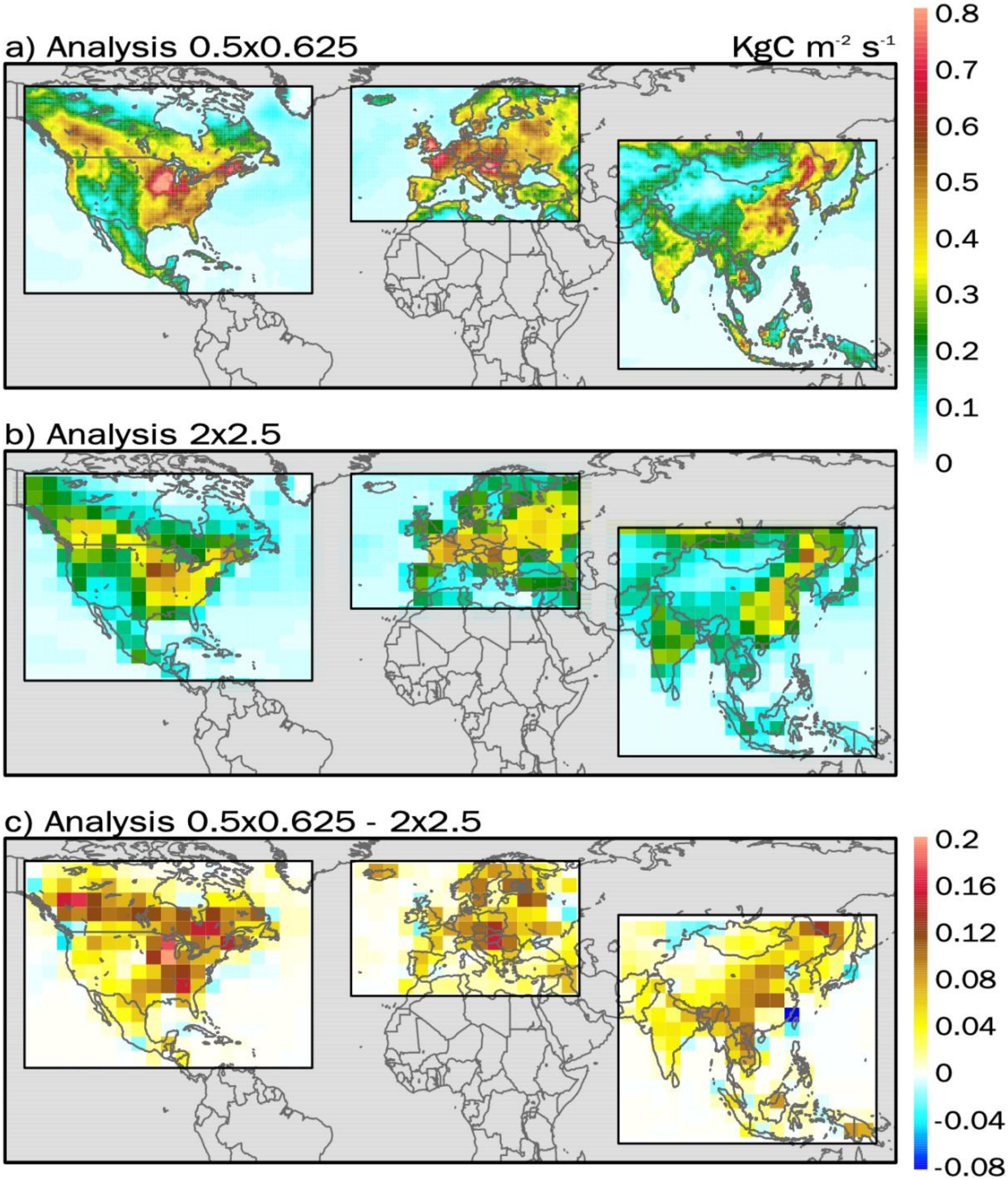

Figure S9: Seasonal strength of terrestrial and ocean carbon fluxes (KgC m^{-2} yr^{-1}) in a) EXP-high and b) EXP-low for 2015~2018. c) The seasonal strength difference between EXP-high and EXP-low.

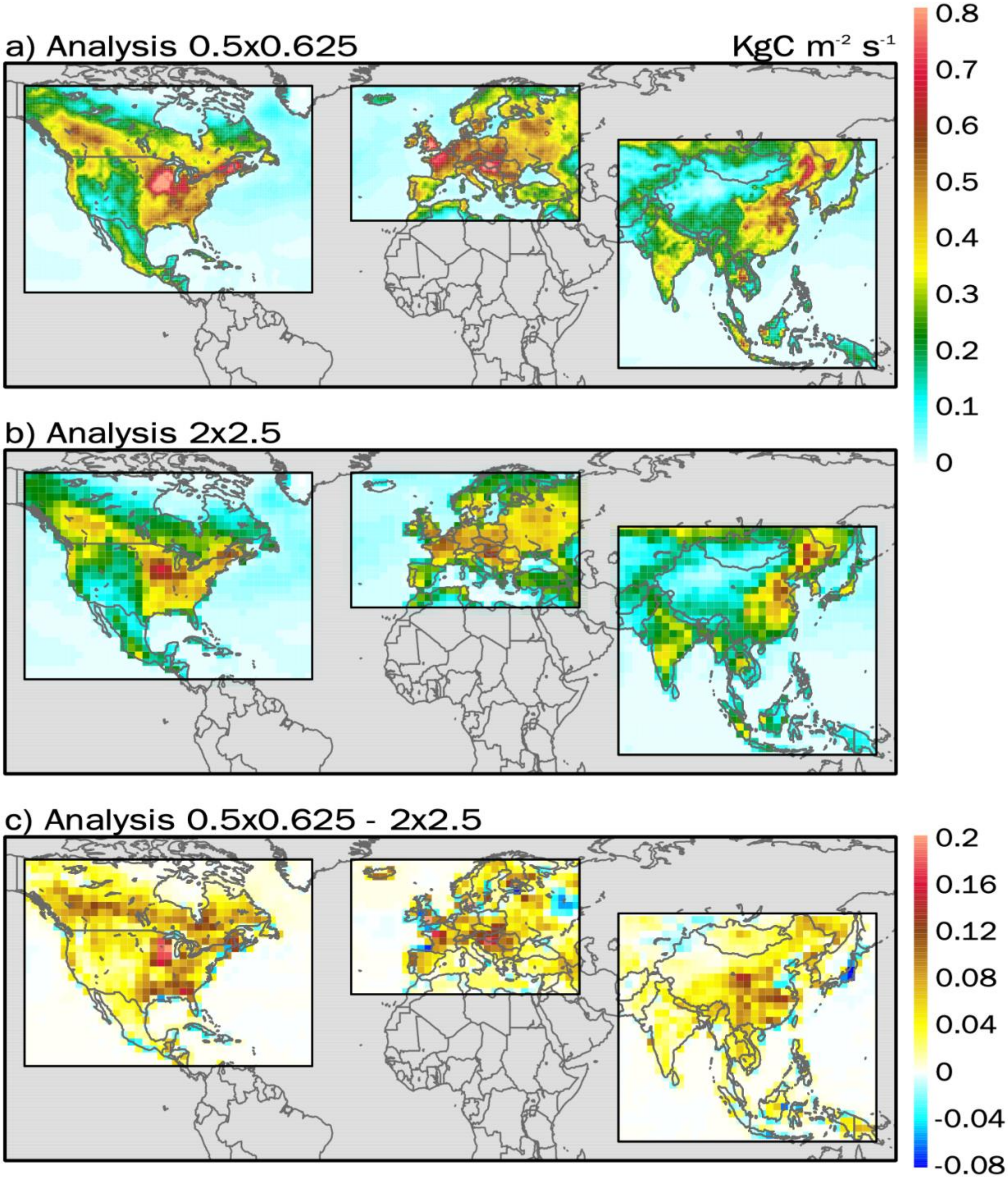

Figure S10: Seasonal strength of terrestrial and ocean carbon fluxes (KgC m^{-2} yr^{-1}) in a) EXP-high and b) EXP-mid for 2015~2018. c) The seasonal strength difference between EXP-high and EXP-mid.

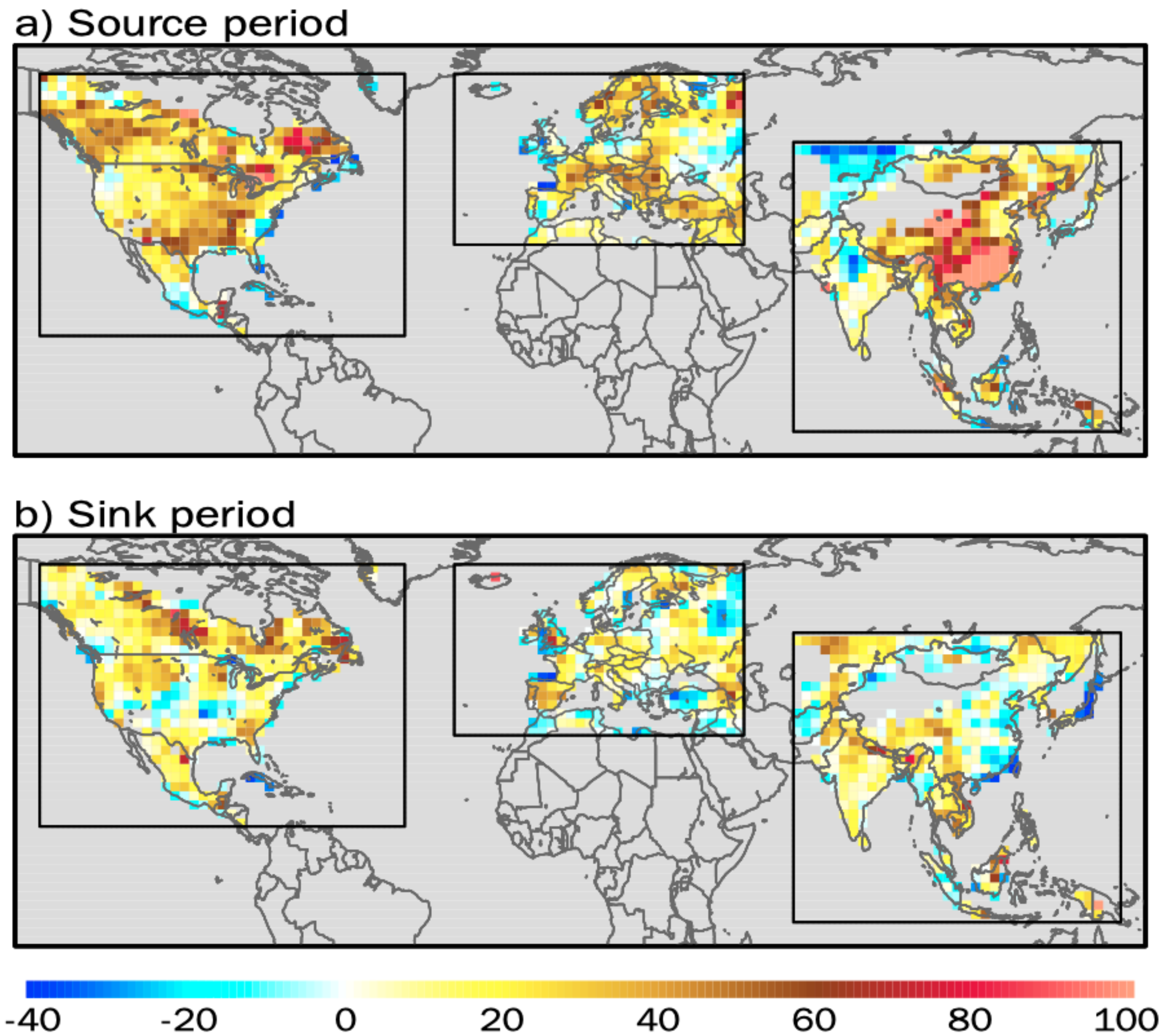

Figure S11: Same as Fig. 2, but for the EXP-high compared with EXP-mid.

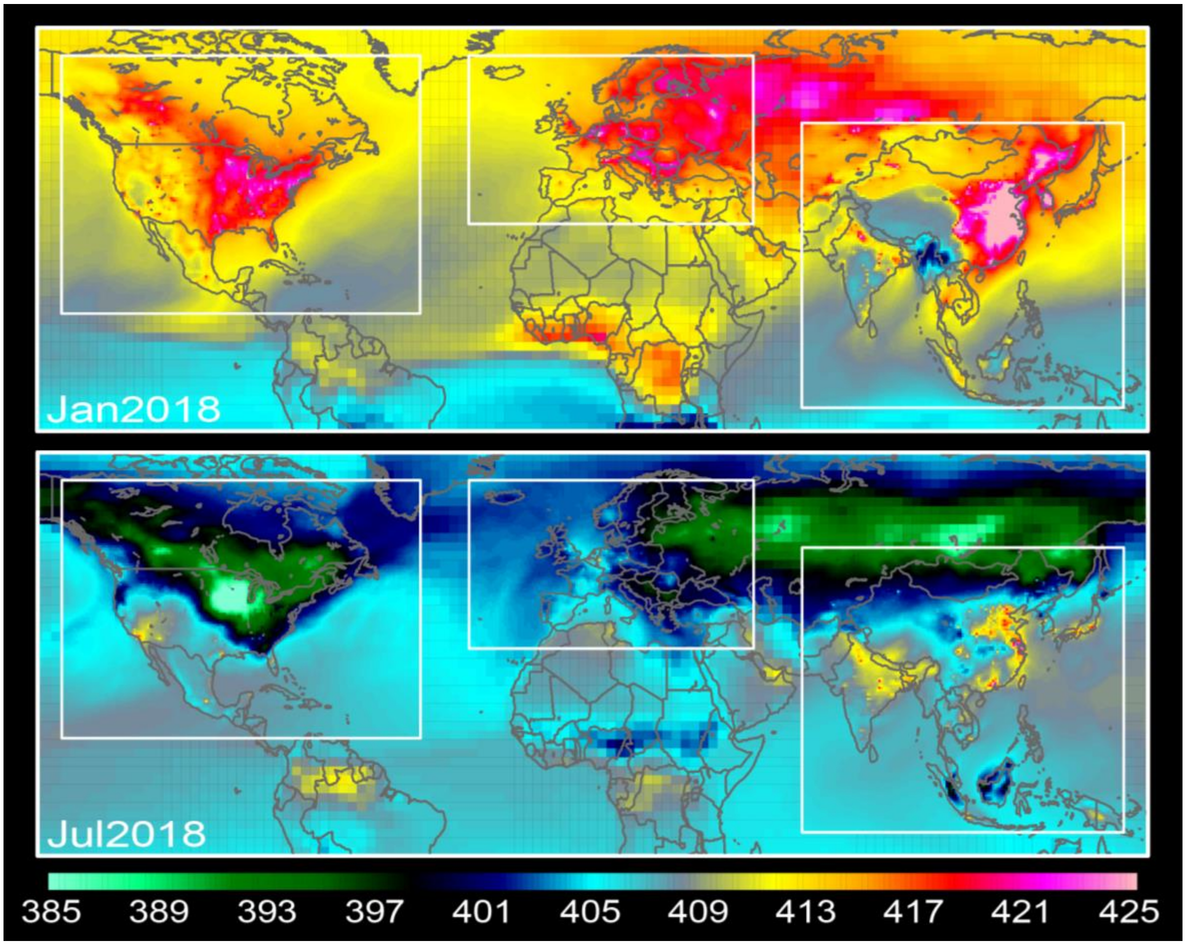

Figure S12: The monthly mean surface CO_2 distribution of ensemble mean (ppm) on January 2018 and July 2018. The CO_2 within the three white squares is the result of EXP-high at 0.5° ×0.625° resolution, and the CO_2 outside the squares is the result of EXP-mid at 2° ×2.5° resolution.

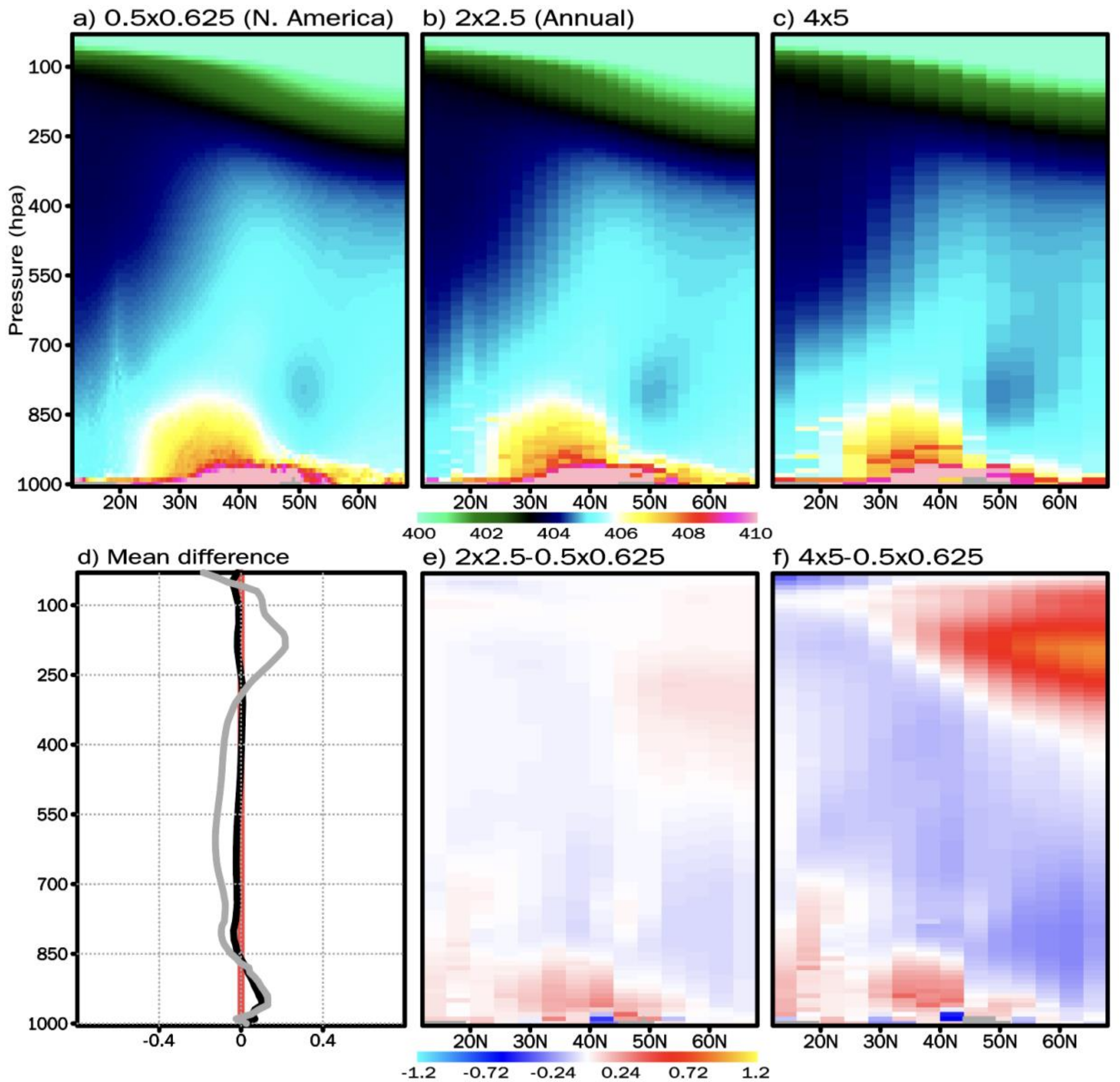

Figure S13: a-c) The 4-year mean vertical-latitude CO_2 distribution (ppm) in N. America for EXP-high, EXP-mid, and EXP-low, respectively. They were averaged within the longitude band of -105 °W~65 °W. d) The vertical bias of EXP-mid (black) and EXP-low (gray) compared to EXP-high, which has been averaged within the latitude band in a-c. e,f) The vertical-latitude CO_2 bias of EXP-mid and EXP-low compared to EXP-high.

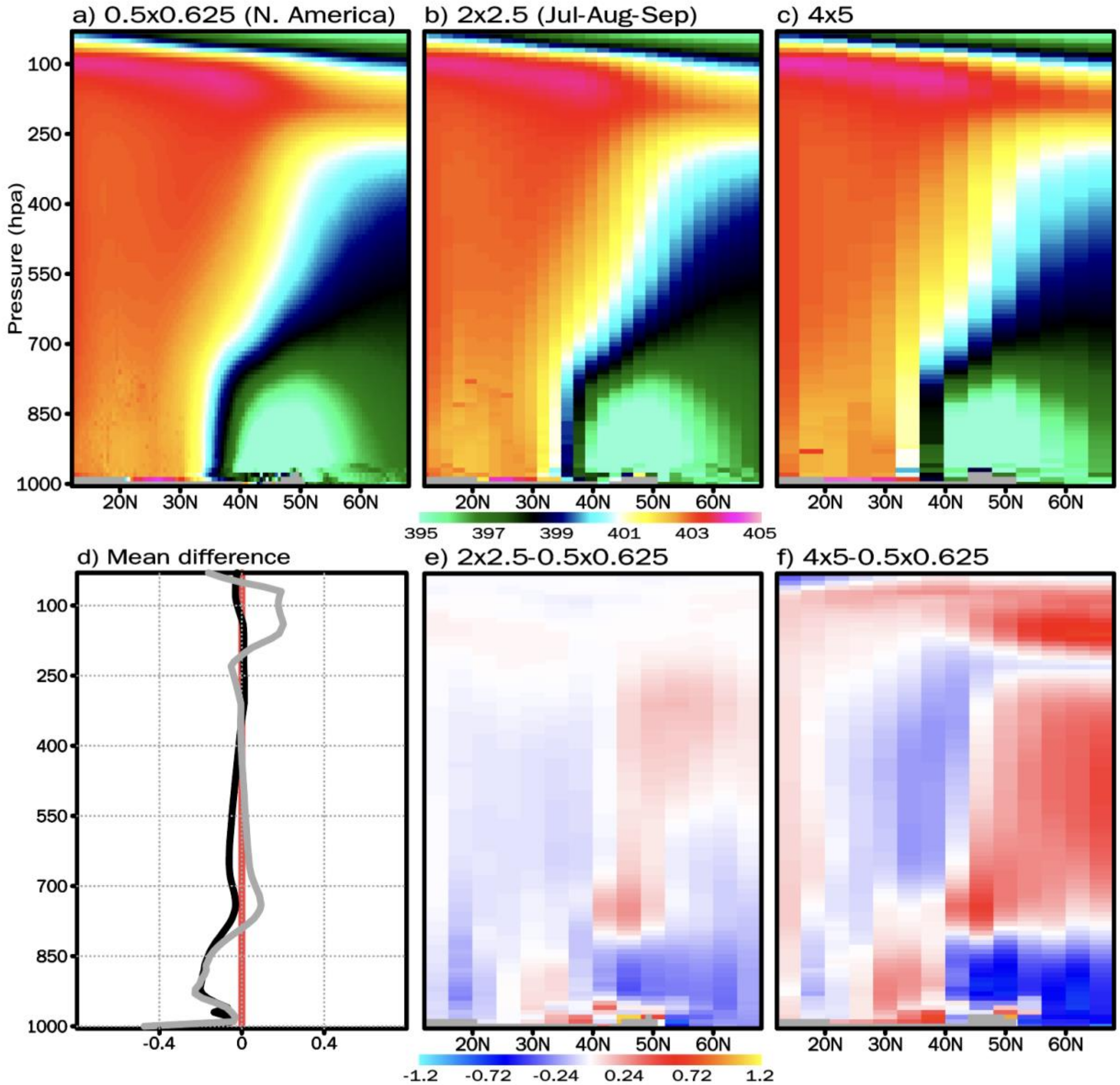

Figure S14: Same as Fig. S2, but for the growing season from July to September.

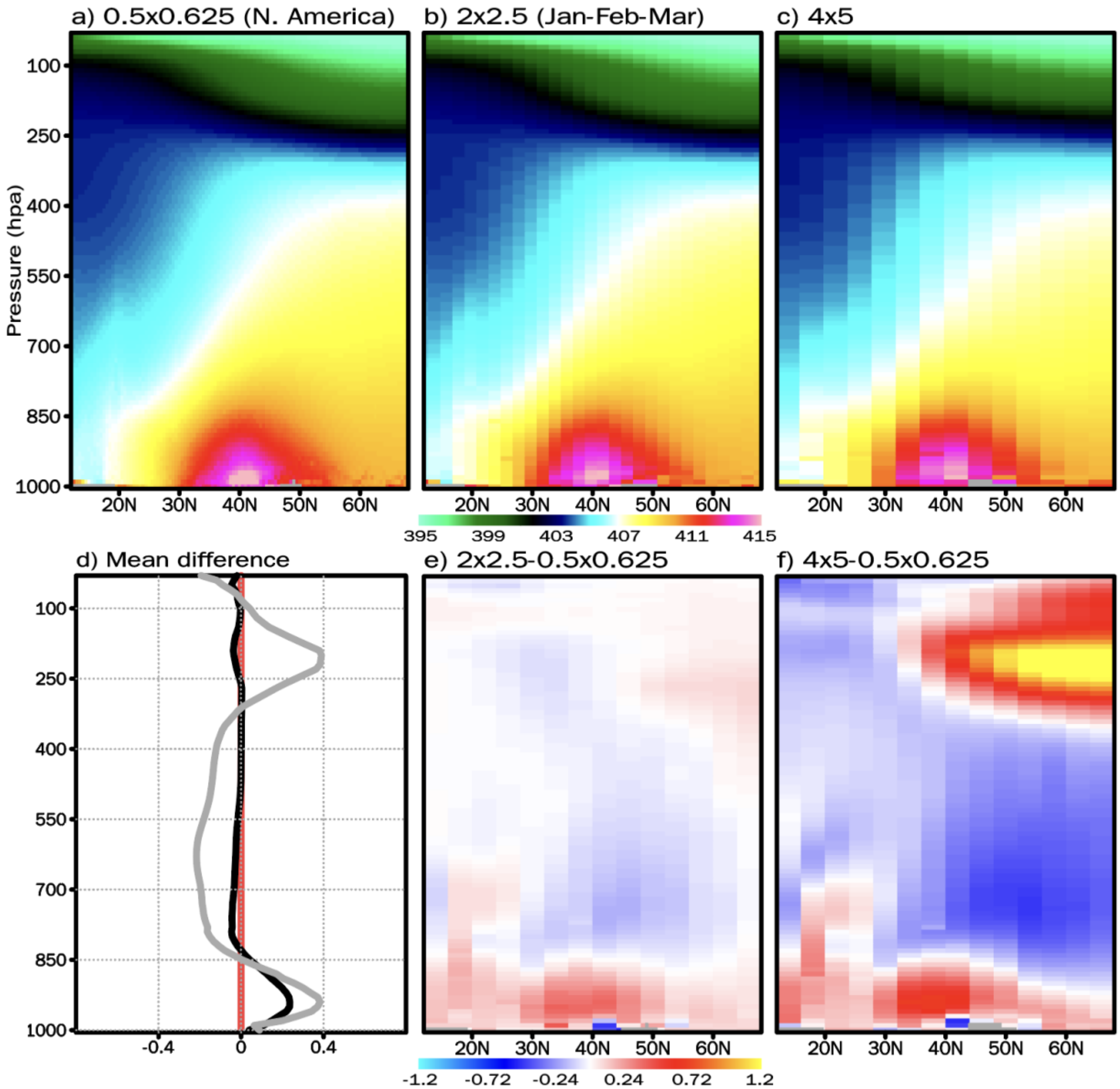

Figure S15: Same as Fig. S2, but for the decaying season from January to March.

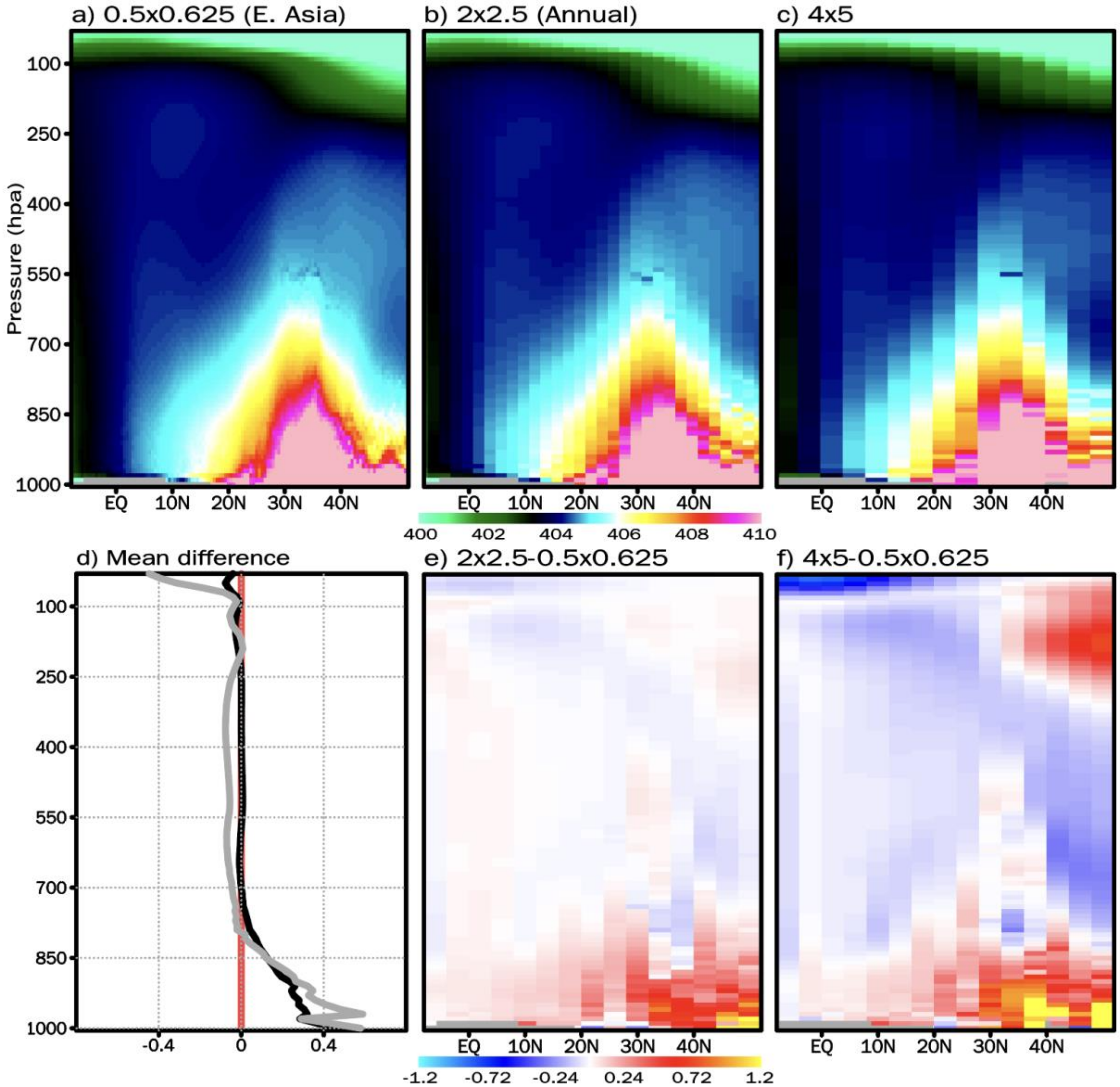

Figure S16: Same as Fig. S2, but in the E. Asia. The longitude band ranges from 65 °E~135 °E.

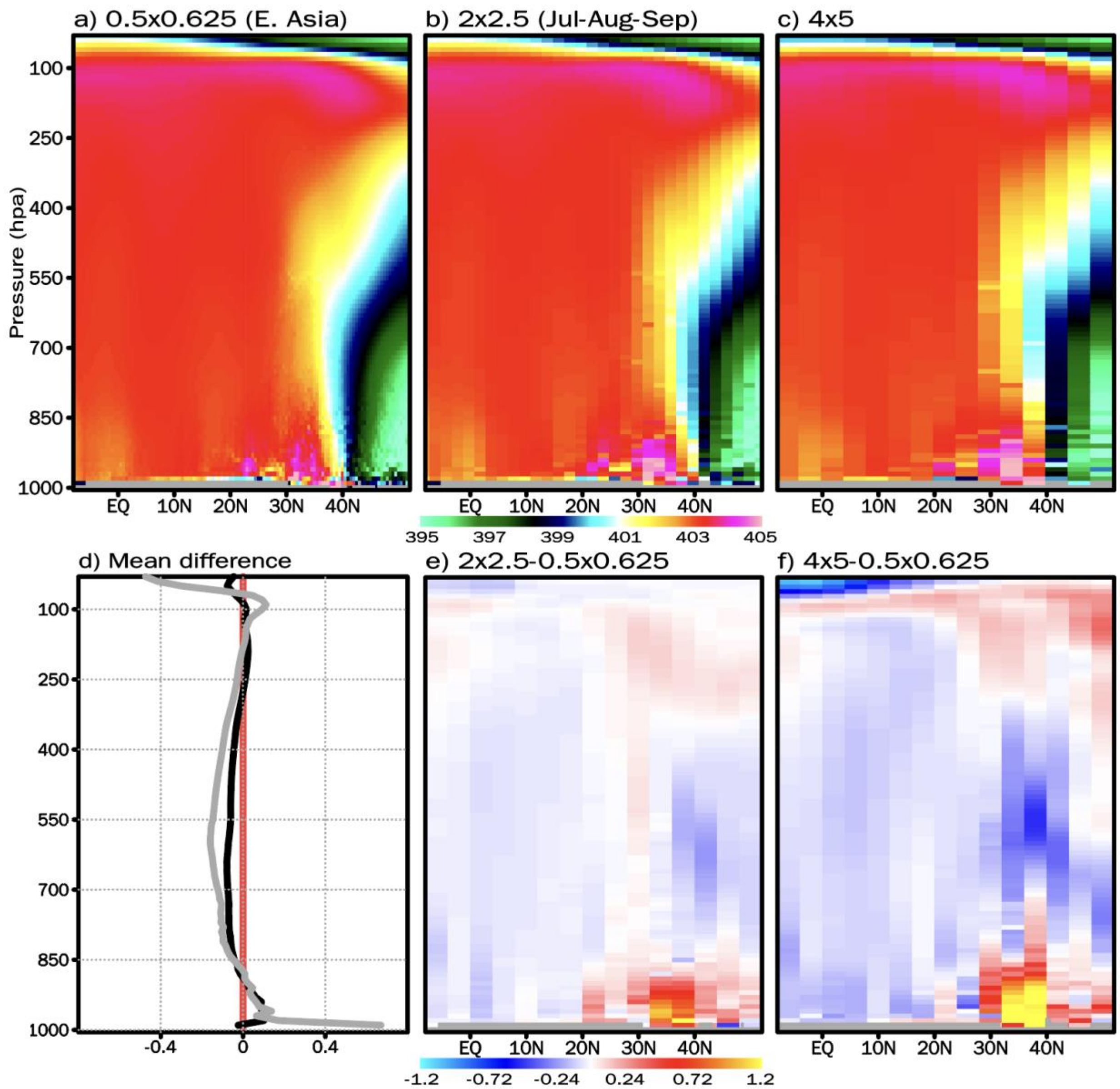

Figure S17: Same as Fig. S5, but for the growing season from July to September.

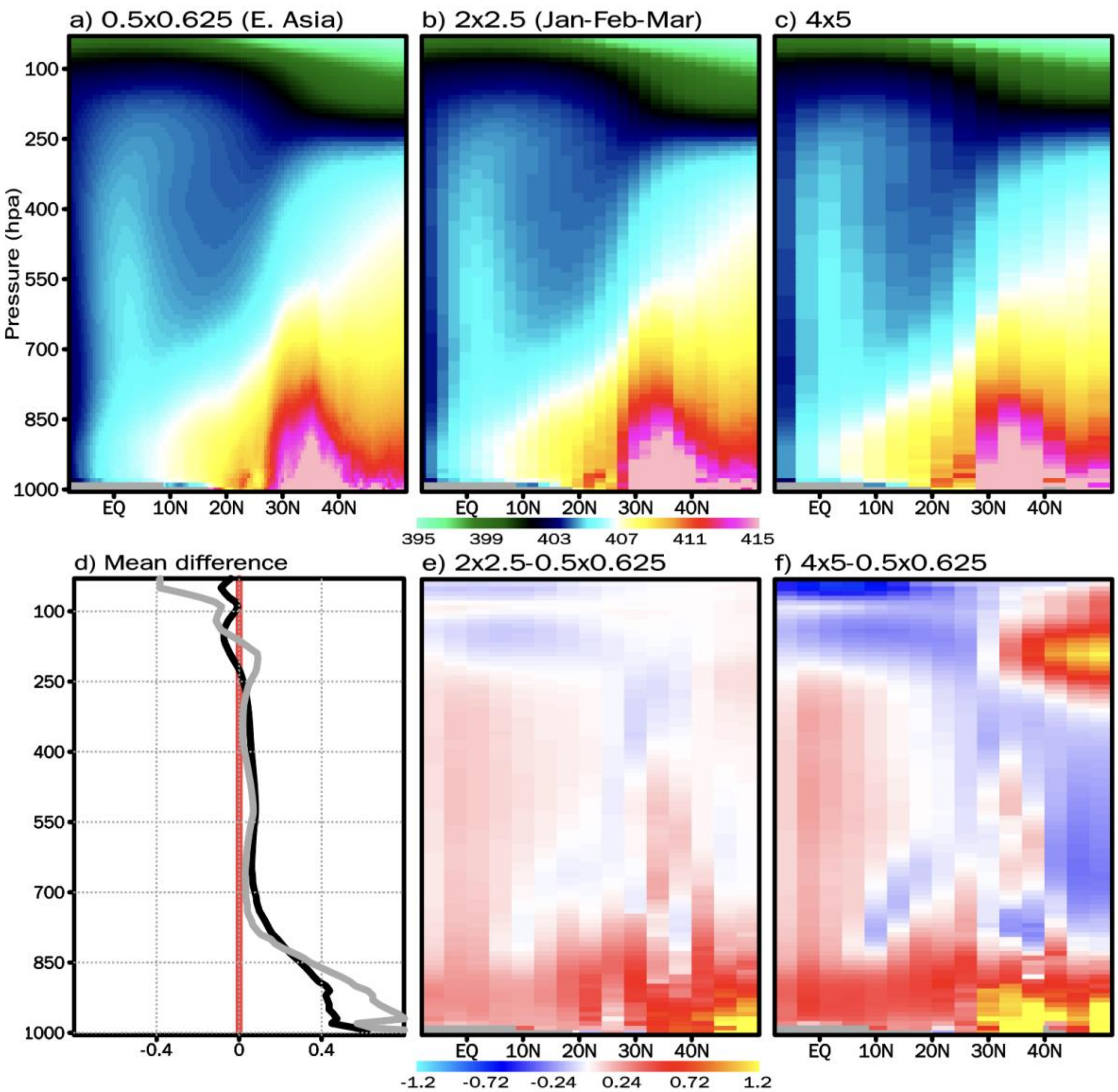

Figure S18: Same as Fig. S5, but for the decaying season from January to March.

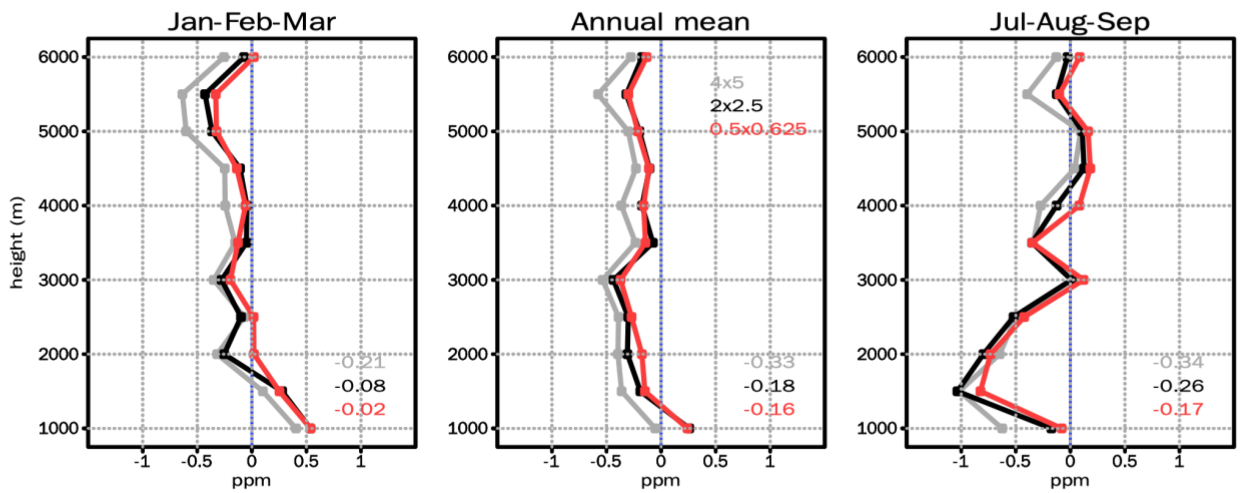

Figure S19: The mean vertical CO_2 biases in EXP-high, EXP-mid, and EXP-low compared to 6 vertical CO_2 profiles (car, hil, cma, crv, esp, and etl) above N. America.